MODELLING OF FIRE RESISTANCE AND MECHANICAL PERFORMANCE OF GLASS FAÇADES

KIM MEOW LIEW[1,2], WEIKANG SUN[1], BINBIN YIN[1,2],
JINHUA SUN[3] & VENKATESH KUMAR R. KODUR[4]
[1]Department of Architecture and Civil Engineering, City University of Hong Kong, China
[2]Centre for Nature-Inspired Engineering, City University of Hong Kong, China
[3]Thermal Science and Energy Engineering, The University of Science and Technology of China, China
[4]Department of Civil and Environmental Engineering, Michigan State University, USA

ABSTRACT

Glass façades are widely used in modern high-rise buildings because of their aesthetic merits and environmentally friendly characteristics. However, collapsing glass in an accidental fire can lead to huge casualties and economic losses. Here, we develop a meshfree computational framework based on peridynamics to investigate the fire resistance and mechanical performance of glass façades. The proposed model is well verified and applied to explore the damage and failure mechanisms of glass façades. The effects of the temperature distribution on the thermomechanical fracture behaviour of glazing are also explored. Results show that cracks tend to initiate at fixed supporting points such as bolts and their propagation paths are greatly influenced by the temperature distributions. Both temperature gradient and local boundary conditions can play a significant role in the thermomechanical cracking of glass façades. This work provides important insights on cracking mechanisms of glass façades during a fire and provide the building and construction companies with new recommendations and design guidelines for improved fire safety.

Keywords: meshless, modelling, fire resistance, mechanical performance, glass façade.

1 INTRODUCTION

Research interest in glazing protection from fire has been growing with the wide application of glass façades in modern high-rise buildings. Glass façade breakage during a fire induces more fresh air to enter the structure, causing catastrophic consequences [1]. To avoid such hazardous scenarios, understanding and predicting the thermomechanical behaviours of glass façades is crucial. Various experimental setups have been adopted to study the heat transfer and breakage processes of different types of glass [2], [3] under diverse fixation conditions [4], [5] during a fire event. However, full-scale experiments are expensive and require many precautions, particularly for the full-field measurements of temperature and displacement during a fire incident. Therefore, an effective and accurate computational framework is urgently demanded to simulate and predict the thermomechanical behaviours of glass façades.

Several numerical methods have been applied to study the heat transfer mechanisms, such as the finite element method (FEM) [6] and the finite volume method (FVM) [7]. However, these grid-based methods face huge challenges when discontinuity (e.g., crack) occurs in the problem domain. Phase field method has shown its calibre in modelling crack propagation in materials, whereas the correct modelling of multiple cracks relies on local mesh update and refinement [8]. Without mesh issues, meshfree methods have been developing fast in the past decades [9]–[13]. As a nonlocal model, peridynamics (PD) is increasingly used to simulate fracture initiation and propagation in both homogeneous and heterogeneous materials [14]–[17] under various loading conditions [18], [19]. However, few works were reported to apply peridynamics in modelling fire-induced structural failures, particularly, the crack propagation in glass façades during fire events.

WIT Transactions on Engineering Sciences, Vol 135,
www.witpress.com, ISSN 1743-3533 (on-line)
doi:10.2495/BE460071

To fill this gap, we propose a three-dimensional peridynamic framework to model the thermomechanical behaviours of glass façades. In our PD method, the governing equations for the mechanical problem, heat transfer problem, and their coupled problem are formulated in integral forms, which naturally incorporate the discontinuity scenarios. Two test cases are presented to demonstrate the effectiveness of the proposed method for modelling thermomechanical deformation and cracking in glass façade.

2 COMPUTATIONAL FRAMEWORKS

2.1 Peridynamic framework

In PD theory, two particles can have a non-local interaction with each other from a finite distance. The major variables in PD theory are shown in Fig. 1.

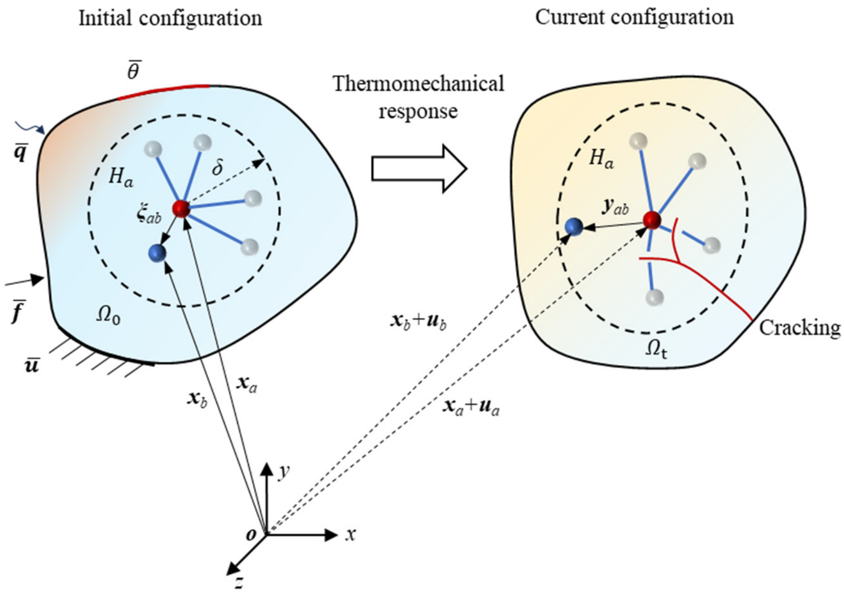

Figure 1: Illustration of variables used in PD framework.

As displayed in Fig. 1, it is assumed in PD that for any given particle (or material point), there is a positive number δ, called the horizon, such that

$$|\boldsymbol{\xi}_{ab}| > \delta \Rightarrow \boldsymbol{f}(\boldsymbol{\xi}_{ab}, \boldsymbol{\eta}_{ab}) = \boldsymbol{0}, \text{ for } \forall \boldsymbol{\xi}_{ab}, \tag{1}$$

where $\boldsymbol{f}$ is the pairwise bond force per unit volume, $\boldsymbol{\xi}_{ab}$ and $\boldsymbol{\eta}_{ab}$ are the relative position and displacement vectors in the reference configuration, which can be written as

$$\boldsymbol{\xi}_{ab} = \boldsymbol{x}_b - \boldsymbol{x}_a, \qquad \boldsymbol{\eta}_{ab} = \boldsymbol{u}_b - \boldsymbol{u}_a. \tag{2}$$

By applying the Newton's second law, the equation of motion in PD can be written as

$$\rho_a \ddot{\boldsymbol{u}}_a = \int_{\mathcal{H}_a} \boldsymbol{f}(\boldsymbol{\xi}_{ab}, \boldsymbol{\eta}_{ab})\, dV_b + \boldsymbol{b}_a \tag{3}$$

where ρ_a and $\ddot{\boldsymbol{u}}_a$ are the mass density and acceleration of particle a, dV_b is the volume of particle b in the family of particle a (denoted as $\mathcal{H}_a$), and $\boldsymbol{b}_a$ is the external body force applying on particle a.

For an isotropic linear elastic material,

$$\boldsymbol{f}(\boldsymbol{\xi}_{ab},\boldsymbol{\eta}_{ab}) = cs_{ab}\cdot[1-d(\boldsymbol{\xi}_{ab},\boldsymbol{\eta}_{ab})]\cdot\widehat{\boldsymbol{y}_{ab}}, \tag{4}$$

where the unit deformed bond vector

$$\widehat{\boldsymbol{y}_{ab}} = \frac{\boldsymbol{y}_{ab}}{y_{ab}}, \boldsymbol{y}_{ab} = \boldsymbol{\xi}_{ab}+\boldsymbol{\eta}_{ab}, y_{ab} = |\boldsymbol{y}_{ab}| = \lambda_{ab}|\boldsymbol{\xi}_{ab}|, \tag{5}$$

and the bond strain and bond stretch are

$$s_{ab} = (\lambda_{ab}-1), \lambda_{ab} = \frac{|\boldsymbol{y}_{ab}|}{|\xi_{ab}|}. \tag{6}$$

In eqn (4), c is micro-modulus (or bond stiffness) and $d(\boldsymbol{\xi}_{ab},\boldsymbol{\eta}_{ab})$ is the bond damage (i.e., $d = 0$ for intact and 1 for broken). The material parameter c can be calibrated with classical theory on the basis of energy equivalence under the small deformation assumption [20], [21] as

$$c = \frac{14E}{\pi\delta^4}\left[1-\left(\frac{|\xi_{ab}|}{\delta}\right)^2\right]^2, \tag{7}$$

for 3D cases, where E is the Young's modulus, v is the Poisson's ratio and h is the thickness of the body in a 2D problem. The bond damage $d(\boldsymbol{\xi}_{ab},\boldsymbol{\eta}_{ab})$ is defined as

$$d(\boldsymbol{\xi}_{ab},\boldsymbol{\eta}_{ab}) = \begin{cases} 0 & if\ s_{ab} < s_c, \\ 1 & if\ s_{ab} \geq s_c, \end{cases} \tag{8}$$

where s_c is the critical bond stretch, which can be calibrated using linear fracture mechanics parameter (i.e., the critical energy release rate G_c) [20], [21] or the tensile strength σ_b (used in this work) or their minimum value as

$$s_c = \min\left(\frac{\sigma_b}{E}, \sqrt{\frac{1024\pi G_c}{7(120\pi-133)E\delta}}\right). \tag{9}$$

The damage of a particle a can be further defined as

$$D_a = \frac{\sum_{b=1}^{Na} d(\xi_{ab},\eta_{ab})}{N_a}, \tag{10}$$

where $d(\boldsymbol{\xi}_{ab},\boldsymbol{\eta}_{ab})$ is the bond damage defined in eqn (8) and N_a is the number of total bonds in the family of particle a.

2.2 PD for heat transfer

To derive the PD version of heat transfer equation, we first recall the energy balance equation for a purely heat transfer process

$$\int_\Omega \rho c_v \frac{\partial\theta}{\partial t}dv = -\int_{\partial\Omega}\boldsymbol{q}\cdot\boldsymbol{n}\,da + \int_\Omega q_s\,dv, \tag{11}$$

where ρ is the mass density, c_v is the specific heat capacity, $\boldsymbol{q}$ is the heat flux, $\boldsymbol{n}$ is the unit surface normal vector and q_s is the source term for heat generation. Applying the divergence theorem and the Fourier's law for heat conduction $\boldsymbol{q} = -\kappa \boldsymbol{\nabla} \theta$ (κ is the heat conduction coefficient), we have the local form of heat transfer equation

$$\rho c_v \frac{\partial \theta}{\partial t} = \kappa \Delta \theta + q_s. \tag{12}$$

In PD theory, we have

$$\rho_a c_v \frac{\partial \theta_a}{\partial t} = \int_{\mathcal{H}_a} K(\boldsymbol{x}_a, \boldsymbol{x}_b) \frac{\theta_b - \theta_a}{\|x_b - x_a\|^2} dV_b + h_s, \tag{13}$$

where $K(\boldsymbol{x}_a, \boldsymbol{x}_b)$ is the heat conduction coefficient of PD thermal bond between particles *a* and *b*, and h_s is the source term of heat generation per unit mass. By drawing an equivalence between PD and classical heat flux, $K(\boldsymbol{x}_a, \boldsymbol{x}_b)$ can be calibrated and expressed with classical parameter *k*. For 3D cases, $k_0 = 9\kappa/(2\pi\delta^3)$ and $k_1 = 18\kappa/(\pi\delta^3)$.

2.3 Initial and boundary conditions

In terms of heat transfer, the initial condition can be implemented directly on each PD particles as

$$\theta_a(\boldsymbol{x}, t)|_{t=0} = \theta_0(\boldsymbol{x}). \tag{14}$$

A uniform Dirichlet boundary condition will also be used in this work, which can be written as

$$\theta(\boldsymbol{x}, t)|_{x \in \Omega_d} = \theta^*. \tag{15}$$

where θ^* is again the prescribed temperature at the Dirichlet boundary $\boldsymbol{x}=\boldsymbol{x}^*$ and Ω_d is the Dirichlet boundary layer generated by mirroring PD particles symmetric to $\boldsymbol{x}=\boldsymbol{x}^*$.

Whereas the Neumann boundary conditions will be modified before applied to boundary PD particles in Neumann boundary layers Ω_n. The principle of modification is to assume that the heat flux $\boldsymbol{q}$ is uniform through the thickness Δ of boundary layer and then the heat generation per unit volume can be derived from the heat flux according to the energy balance law

$$\int_{\Omega_n} \rho_a c_v \frac{\partial \theta_a}{\partial t} dV_a = -\int_{\partial \Omega_n} \boldsymbol{q} \cdot \boldsymbol{n} \, dS_a, \tag{16}$$

as

$$\rho_a c_v \frac{\partial \theta_a(x,t)}{\partial t}|_{x \in \Omega_n} = -\frac{\boldsymbol{q} \cdot \boldsymbol{n} S_a}{V_a} = -\frac{\boldsymbol{q} \cdot \boldsymbol{n}}{\Delta}. \tag{17}$$

Particularly, for convective boundary conditions

$$\rho_a c_v \frac{\partial \theta_a(x,t)}{\partial t}|_{x \in \Omega_n} = \frac{h}{\Delta}(\theta_\infty - \theta_a), \tag{18}$$

where θ_∞ is the temperature of surrounding medium, and h is the convective heat transfer coefficient.

Furthermore, for radiation boundary conditions

$$\rho_a c_v \frac{\partial \theta_a(x,t)}{\partial t}|_{x \in \Omega_n} = \frac{\varepsilon \sigma}{\Delta}(\theta_s^4 - \theta_a^4), \tag{19}$$

where θ_s is the temperature of the surface surrounding the body, ε is emissivity of the boundary surface and σ is the Stefan–Boltzmann constant.

On the other hand, the mechanical initial and boundary conditions are rather straight forward (applying displacement, velocity and body force on boundary particles) [16].

2.4 Thermomechanical coupling

Thermomechanical coupling has two aspects, i.e., thermal strain (from temperature field to strain field) and mechanical heating (from strain rate field to temperature field). In this work, only the former one is considered. By inserting the thermal strain into eqn (4), the governing equation can be rewritten as

$$\rho_a \ddot{\boldsymbol{u}}_a = \int_{\mathcal{H}_a} c(s_{ab} - \alpha\theta_{avg}) \cdot [1 - d(\boldsymbol{\xi}_{ab}, \boldsymbol{\eta}_{ab})] \cdot \widehat{\boldsymbol{y}_{ab}}\, dV_b + \boldsymbol{b}_a, \tag{20}$$

where α is the thermal expansion coefficient

$$\theta_{avg} = \frac{\theta_a + \theta_b}{2}, \tag{21}$$

and other variables are given in eqns (5)–(8).

3 RESULTS AND DISCUSSION

3.1 Verification test example

This test case is aimed to verify the PD method for modelling thermomechanical deformation.

As shown in Fig. 2, the side length of the square is L = 1 cm. The initial temperature is θ_0 = 0°C. The lateral displacement of left and right sides of the square are constrained. The vertical motion of the bottom side of the square is also constrained. A thermal shock of θ_1 = 1°C is applied to the upper side of the square. The Young's modulus of the square is 1 GPa, Poisson's ratio is 0.33, thermal expansion coefficient is 0.02/K, thermal conductivity is 1 W/(m·K) and specific heat capacity is 1 J/(kg·K).

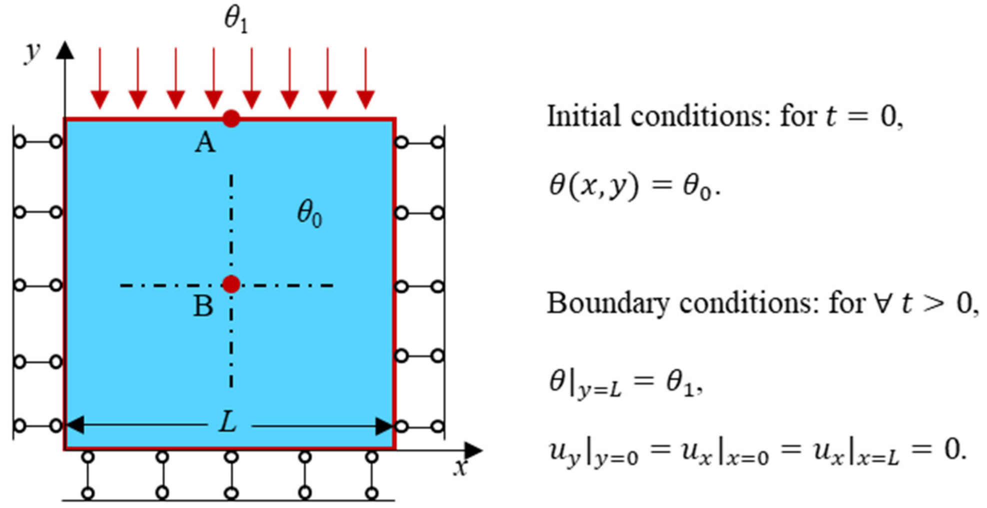

Figure 2: Test setup of the square plate under thermal shock.

The displacement history at point A and the temperature history at point B marked in Fig. 2 are given in Fig. 3. The temperature increase is nonlinear over time. With the increase of spatial resolution, PD results show greater agreement with the analytical results presented in Chen et al. [22], confirming the convergence and accuracy of the proposed PD method.

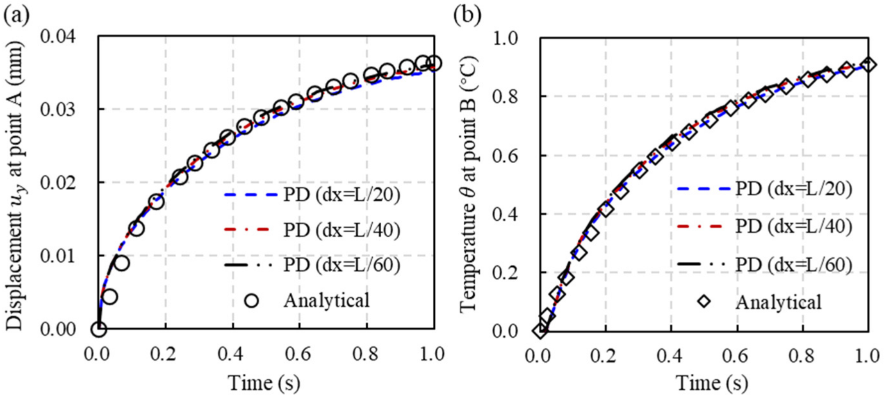

Figure 3: Comparison of PD and analytical results of displacement at point A and temperature history at point B.

3.2 Effects of temperature distribution on the fracture pattern of glazing

To explore the effect of temperature distribution and fixture forms, a square single glazing with side length of 1.2 m, thickness of 6 mm and four-point fixture (by bolts) was studied. As shown in Fig. 4, the distance between two bolts *D* is 0.2 m and three levels of the width of high temperature zone *H* = *L*/4, *L*/3 and *L*/2 are adopted. The Young's modulus of the glazing is 67 GPa, Poisson's ratio is 0.25, tensile strength is 40 MPa, and thermal expansion coefficient is 8.5×10^{-6}/K. Temperature increasing rates are 1.2 and 0.5 K/s for high and low temperature zones respectively. The horizon radius is 3.015 times the initial particle spacing. A total number of 121,203 particles are used in this example.

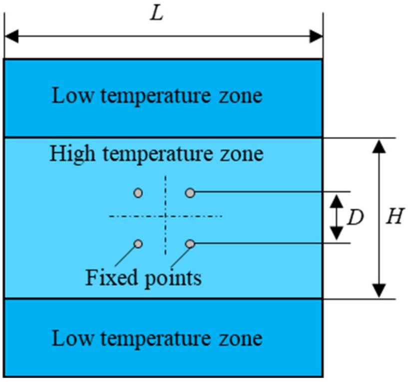

Figure 4: Test setup of the square single glazing. (a) Temperature distribution; and (b) Geometry.

The crack patterns of the glazing with different temperature distributions are presented in Fig. 5. As can be observed, crack initiates at the fixed points for all the three test cases. However, once initiated, the crack propagation paths are remarkably different for different widths of the high-temperature zone. For the case of $H = L/4$, initiated cracks first grow into two parallel cracks in the direction vertical to the two temperature–transition interfaces. After these cracks meet the two interfaces, they propagate along the interfaces until they fully penetrate the glazing. For the case of $H = L/3$, the crack pattern is quite similar despite that the cracks form curved paths instead straight ones before meeting the temperature–transition interfaces. For the case of $H = L/2$, the crack pattern is much more complex. Cracks not only form bended paths before meeting the temperature–transition interfaces they also merge into a straight path parallel to the temperature–transition interfaces. In addition, the cracks at the temperature–transition interfaces bifurcate before penetrating the glazing. These results imply that both the mechanical factors (e.g., point supports or frame supports) and the thermal factors (e.g., the temperature distribution and gradient) play significant roles in the cracking mechanisms of glass façades.

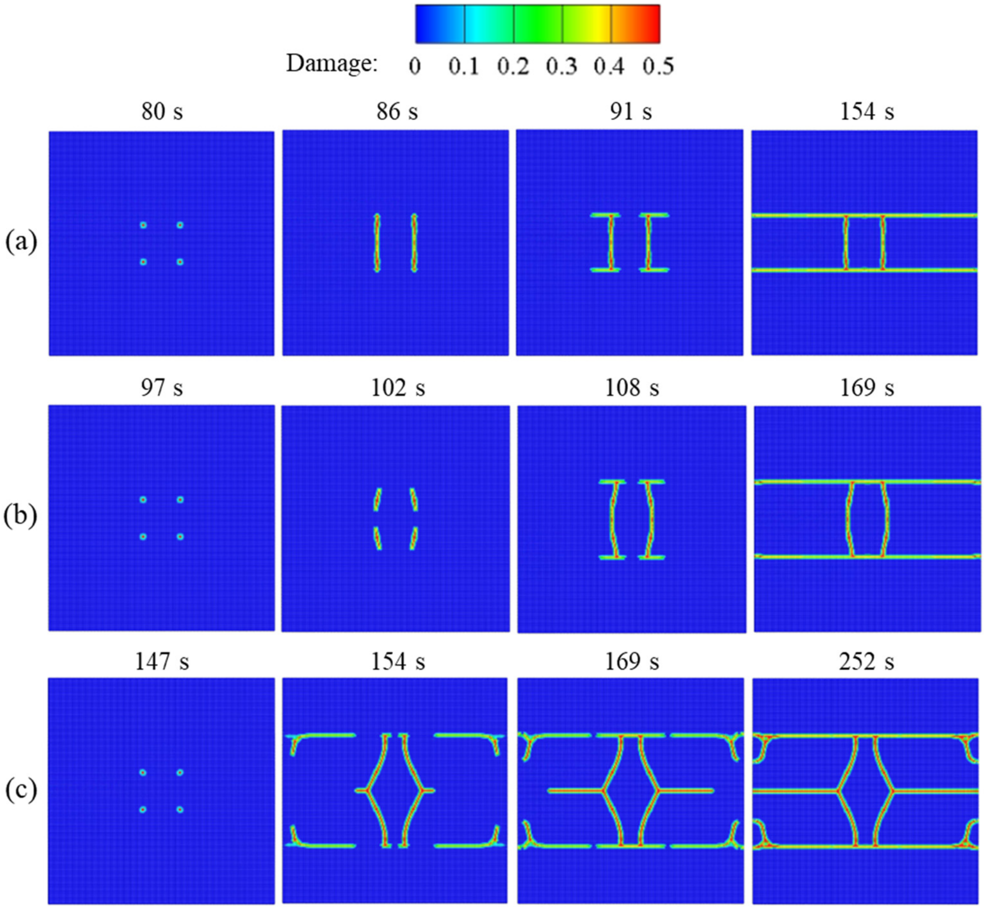

Figure 5: Crack evolution processes of the square glazing of different temperature distribution with (a) $H = L/4$; (b) $H = L/3$; and (c) $H = L/2$.

4 CONCLUSIONS

In this paper, we present a peridynamic framework to simulate the thermomechanical behaviours of glass façades exposed to fire. The computational effectiveness and accuracy of our PD method was verified by the thermomechanical deformation of a square plate. The proposed PD method was applied to explore the effect of temperature distribution on the crack patterns of glazing. Results indicate that both the mechanical factors such as point supports and the thermal factors like the temperature gradient play significant roles in the cracking of glass façades. To predict the thermomechanical and fracture behaviour of glass façades more accurately, the realistic boundary conditions at supporting frame or fixed points should be carefully considered and the temperature distribution in the glazing should be accurately measured or modelled.

ACKNOWLEDGEMENT

The authors gratefully acknowledge the supports provided by the Research Grants Council of the Hong Kong Special Administrative Region, China (Project No. 9043135, CityU 11202721).

REFERENCES

[1] Bedon, C., Structural glass systems under fire: overview of design issues: Experimental research and developments. *Advances in Civil Engineering*, 2120570, 2017.

[2] Wang, Y., Wang, Q., Sun, J., He, L. & Liew, K.M., Influence of fire location on the thermal performance of glass façades. *Applied Thermal Engineering*, **106**, pp. 438–442, 2016.

[3] Wang, Y., Wang, Q., Wen, J.X., Sun, J. & Liew, K.M., Investigation of thermal breakage and heat transfer in single, insulated and laminated glazing under fire conditions. *Applied Thermal Engineering*, **125**, pp. 662–672, 2017.

[4] Wang, Y. et al., Experimental study on thermal breakage of four-point fixed glass façade. *Fire Safety Science: Proceedings of the Eleventh International Symposium, IAFSS*, Christchurch, New Zealand, pp. 666–676, 2014.

[5] Wang, Y. et al., Numerical study on fire response of glass façades in different installation forms. *Construction and Building Materials*, **61**, pp. 172–180, 2014.

[6] Bakalakos, S., Kalogeris, I. & Papadopoulos, V., An extended finite element method formulation for modeling multi-phase boundary interactions in steady state heat conduction problems. *Composite Structures*, **258**, 113202, 2021.

[7] Costa, R., Nobrega, J.M., Clain, S. & Machado, G.J., Very high-order accurate polygonal mesh finite volume scheme for conjugate heat transfer problems with curved interfaces and imperfect contacts. *Computer Methods in Applied Mechanics and Engineering*, **357**, 112560, 2019.

[8] Tian, F., Tang, X., Xu, T., Yang, J. & Li, L., A hybrid adaptive finite element phase-field method for quasi-static and dynamic brittle fracture. *International Journal for Numerical Methods in Engineering*, **120**(9), pp. 1108–1125, 2019.

[9] Zhang, L.W., Lei, Z.X. & Liew, K.M., Computation of vibration solution for functionally graded carbon nanotube-reinforced composite thick plates resting on elastic foundations using the element-free IMLS-Ritz method. *Applied Mathematics and Computation*, **256**, pp. 488–504, 2015.

[10] Zhang, L.W. & Liew, K.M., Large deflection analysis of FG-CNT reinforced composite skew plates resting on Pasternak foundations using an element-free approach. *Composite Structures*, **132**, pp. 974–983, 2015.

[11] Zhang, Z., Hao, S.Y., Liew, K.M. & Cheng, Y.M., The improved element-free Galerkin method for two-dimensional elastodynamics problems. *Engineering Analysis with Boundary Elements*, **37**(12), pp. 1576–1584, 2013.

[12] Liew, K.M., Huang, Y.Q. & Reddy, J.N., Moving least squares differential quadrature method and its application to the analysis of shear deformable plates. *International Journal for Numerical Methods in Engineering*, **56**(15), pp. 2331–2351, 2003.

[13] Zhang, Z., Li, D.M., Cheng, Y.M. & Liew, K.M., The improved element-free Galerkin method for three-dimensional wave equation. *Acta Mechanica Sinica*, **28**, pp. 808–818, 2012.

[14] Silling, S.A., Reformulation of elasticity theory for discontinuities and long-range forces. *Journal of the Mechanics and Physics of Solids*, **48**(1), pp. 175–209, 2000.

[15] Silling, S.A., Epton, M., Weckner, O., Xu, J. & Askari, E., Peridynamic states and constitutive modeling. *Journal of Elasticity*, **88**, pp. 151–184, 2007.

[16] Oterkus, S., Madenci, E. & Agwai, A., Fully coupled peridynamic thermomechanics. *Journal of the Mechanics and Physics of Solids*, **64**, pp. 1–23, 2014.

[17] Kilic, B., Peridynamic theory for progressive failure prediction in homogeneous and heterogeneous materials. The University of Arizona, 2008.

[18] Sun, W.K., Zhang, L.W. & Liew, K.M., A coupled SPH-PD model for fluid–structure interaction in an irregular channel flow considering the structural failure. *Computer Methods in Applied Mechanics and Engineering*, **401**, 115573, 2022.

[19] Yin, B.B., Sun, W.K., Zhang, Y. & Liew, K.M., Modeling via peridynamics for large deformation and progressive fracture of hyperelastic materials. *Computer Methods in Applied Mechanics and Engineering*, **403**, 115739, 2023.

[20] Huang, D., Lu, G. & Qiao, P., An improved peridynamic approach for quasi-static elastic deformation and brittle fracture analysis. *International Journal of Mechanical Sciences*, **94**, pp. 111–122, 2015.

[21] Huang, D., Lu, G., Wang, C. & Qiao, P., An extended peridynamic approach for deformation and fracture analysis. *Engineering Fracture Mechanics*, **141**, pp. 196–211, 2015.

[22] Chen, W., Gu, X., Zhang, Q. & Xia, X., A refined thermo-mechanical fully coupled peridynamics with application to concrete cracking. *Engineering Fracture Mechanics*, **242**, 107463, 2021.